Chinese Chemical Letters 37 (2026) 110681

Contents lists available at ScienceDirect

Chinese Chemical Letters

journal homepage: www.elsevier.com/locate/cclet

A "breathable" 3D lithium host with MnO_2 nanoflake array for long-lifespan anode-free lithium metal batteries

Jiaojiao Deng[a], Haocheng Li[b], Fei Zheng[c], Qingsong Weng[c], Yu Bai[c], Xiaoliang Yu[c,*], Qianlin Zhang[a,*], Qinghua Liang[d,*], Baohua Li[e]

[a] Graphene Composite Research Center, College of Chemistry and Environmental Engineering, Shenzhen University, Shenzhen 518060, China
[b] School of Mechanical Engineering, Beijing Institute of Technology, Beijing 100081, China
[c] Department of Mechanical Engineering and Research Institute for Smart Energy, The Hong Kong Polytechnic University, Hong Kong 999077, China
[d] Key Laboratory of Rare Earth, Ganjiang Innovation Academy, Chinese Academy of Sciences, Ganzhou 341000, China
[e] Shenzhen Key Laboratory on Power Battery Safety Research and Shenzhen Geim Graphene Center, Tsinghua Shenzhen International Graduate School, Shenzhen 518055, China

ARTICLE INFO

Article history:
Received 17 October 2024
Revised 25 November 2024
Accepted 25 November 2024
Available online 26 November 2024

Keywords:
Lithium metal battery
Anode free
Nanoflake array
Mechanical breathing
Cycling stability

ABSTRACT

The emerging anode-free lithium metal battery (AFLMB) is very promising for the next-generation electrochemical energy storage technology due to its remarkable high-energy density. However, the current development of AFLMB is seriously hampered by the low Coulombic efficiency and limited lifespan caused mainly by the uncontrolled dendritic lithium growth and significant volume change during Li plating/stripping on the traditional current collector. Here, we report the design of a "breathable" three-dimensional (3D) lithium host with MnO_2 nanoflake array for long-lifespan AFLMB. Specifically, a dense MnO_2 nanoflake array stretchably grown on carbon cloth by an easy solution dipping method is constructed as a 3D current collector for AFLMBs. Both experimental and theoretical studies underlined that the Li_2O/Mn nanoflake arrays produced spontaneously upon the initial lithiation can effectively guide uniform lithium nucleation and growth. Moreover, this unique 3D hierarchical structure expands/shrinks along with the lithium plating/stripping, accommodating the large volume expansion/shrinkage over the subsequent charge/discharge processes. As such, a dendrite-free lithium structure was achieved even at a high capacity of 10 mAh/cm^2. More importantly, the as-constructed AFLMB with this current collector exhibits impressive cycling stability with 64% capacity retained after 200 cycles. This study offers new insights into constructing highly efficient 3D protective layers for metal anodes toward the practical feasibility of anode-free batteries.

© 2025 Published by Elsevier B.V. on behalf of Chinese Chemical Society and Institute of Materia Medica, Chinese Academy of Medical Sciences.

With the increasing energy-storage demand for portable electronics and electrical vehicles, safe and smart battery systems with high energy density and prolonged life are highly desirable [1]. Lithium-metal batteries stand out among various battery technologies since lithium metal anode shows a remarkable theoretical capacity of 3860 mAh/g and a low work potential of −3.04 V (*vs.* standard hydrogen electrode), both enabling an extremely high energy density [2]. In particular, since the pioneering work by Zhang *et al.* [3], the anode-free lithium metal batteries (AFLMBs) constructed with a lithium-containing cathode and a bare anode current collector have attracted tremendous attention among the research community [4,5]. To achieve the working of AFLMB, lithium metal is plated onto the anode current collector during the initial charge process and serves as the lithium source in the subsequent charge/discharge cycles. As such, the air-sensitive lithium metal foil does not need to be used when fabricating the AFLMB. This not only greatly enhances manufacturing safety but also maximizes the energy density of rechargeable AFLMB.

However, the lithium plating/stripping chemistry of AFLMB faces several challenges: (1) The chemically active lithium metal in direct contact with various electrolyte components may result in forming unstable solid electrolyte interphases (SEIs) [6]; (2) Since the lithium deposition is extremely sensitive to the uniformity of Li^+ flux and electric field distribution at the lithium metal surface [7], lithium dendrites enabled by the preferential Li growth at the tips could penetrate the separator and cause severe safety concerns [8]; (3) The large volume swelling/contraction during lithium plating/stripping also causes breaking of the SEI layers and the

* Corresponding authors.
E-mail addresses: xiaoliang.yu@polyu.edu.hk (X. Yu), zhql@szu.edu.cn (Q. Zhang), qhliang@gia.cas.cn (Q. Liang).

https://doi.org/10.1016/j.cclet.2024.110681
1001-8417/© 2025 Published by Elsevier B.V. on behalf of Chinese Chemical Society and Institute of Materia Medica, Chinese Academy of Medical Sciences.

continuous SEI growth, resulting in the continue consumption of electrolytes, dead lithium production, and the reduced Li plating/stripping reversibility [9]; (4) The limited Li source in AFLMB cells imposes pressed requirements for high reversibility, *e.g.*, the AFLMB can sustain 200 cycles at 80% capacity retention if the Coulombic efficiency (CE) is 99.9%, but only 53 and 23 cycles when CE is slightly reduced to 99.5% and 99%, respectively [10]. To promote uniform Li plating/stripping for boosting the Coulombic efficiency of AFLMB, several effective strategies have been proposed in previous studies. For instance, novel electrolytes have been formulated by tuning the electrolyte composition [11–13] and concentration [14] to produce a more rigid and resilient SEI. More attractively, 3D functional lithium hosts like carbon cloth (CC) have been widely developed for AFLMB to accommodate the volume change during Li^+ plating/stripping [15–20]. Functional modifications on lithium metal surfaces have also been proposed *via* electrochemical pretreatment [21,22] or mechanical coatings [23–26] to effectively guide non-dendrite Li growth. Since the repeated and large volume expansion/contraction of the anode during charge/discharge cycles, like mechanical breathing, seriously hinders the electrochemical stability of lithium metal anodes, rational designing of 2D lithium anodes with functional modification layer can accommodate this mechanical stress well along the thickness direction. However, constructing a mechanically compliant modification layer for AFLMB becomes challenging in 3D lithium anodes because of the enormous size variation in three dimensions (Fig. S1a in Supporting information). Modifying the 3D lithium host surface modification by lithiophilic layer is expected to induce uniform lithium deposition at or near the modified surface. Nevertheless, there would still be massive lithium dendrites produced at a high lithium deposition capacity (Fig. S1b in Supporting information). Moreover, this fabrication process is usually complex and costly.

Here, we report a MnO_2 nanoflake array growth on 3D CC as a current collector for long-lifespan AFLMBs. The MnO_2 thin layer was easily grown on CC through a facile solution dipping process at room temperature. Attractively, the MnO_2 layer transforms into Li_2O/Mn nanoflake arrays after lithiation, demonstrating favorable mechanical breathing during lithium plating/stripping processes (Fig. S1c in Supporting information). As such, the Li_2O/Mn nanoflake arrays continuously guide uniform lithium deposition and growth with smooth dendrite-free lithium morphology even at a high lithium plating capacity of 10 mAh/cm^2. More importantly, the as-fabricated AFLMB based on such a current collector displays impressive cycling stability with 64% capacity retained after 200 charge/discharge cycles. This work sheds fresh light on exploiting mechanically breathable 3D modification layers to guide even 3D lithium growth for long-lifespan AFLMBs.

To facilitate the growth of MnO_2, the CC substrate was first treated through two different methods: a vigorous manner by H_2SO_4/HNO_3 refluxing and a mild manner *via* H_2O_2 oxidation. The as-treated CC substrates are designated as CC-v and CC-m, respectively. The surface functional groups on CC substrates after oxidization were detected by Fourier-transform infrared spectroscopy (FTIR). As shown in Fig. 1a, the FTIR spectrum of the pristine CC shows no prominent vibration modes of oxygen functional groups. After a mild H_2O_2 oxidation, a weak peak centered at 1700 cm^{-1} was detected in the FTIR spectrum of CC-m. In the case of H_2SO_4/HNO_3 refluxing-treated CC, stronger peaks centered at 1700, 1580, and 1180 cm^{-1} are identified in the FTIR spectrum of CC-v, indicating the presence of carbonyl groups (−C=O). Meanwhile, the broad peak centered at about 3000 cm^{-1} corresponds to the stretching vibration of –OH [27]. X-ray photoelectron spectroscopy (XPS) has also been conducted for quantitative analysis of surface oxygen functional groups. As summarized in Table S1 (Supporting information), the surface oxygen content of CC, CC-v, and CC-m was determined to be 4.5, 6.2, and 10.6 wt%, respectively.

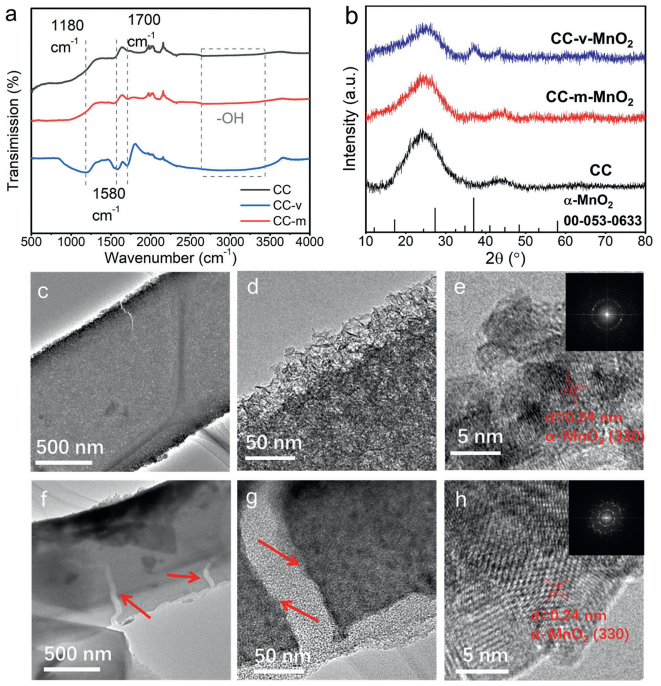


Fig. 1. The structural characterization of CC, CC-v-MnO_2, and CC-m-MnO_2 samples. (a) FTIR spectra of the pristine CC and two treated CC substrates. (b) XRD patterns of CC, CC-v-MnO_2, and CC-m-MnO_2. TEM images of (c-e) CC-v-MnO_2 and (f-h) CC-m-MnO_2 at different magnifications. The insets in (e) and (h) correspond to the SAED patterns.

The treated CC substrates were then dipped into a $KMnO_4$ solution to *in-situ* grow MnO_2. The spontaneous redox reaction between the surface functional groups of modified CC and $KMnO_4$ gives rise to the formation of CC-MnO_2 composites. The corresponding sample is designated CC-v-MnO_2 and CC-m-MnO_2, respectively. X-ray diffraction (XRD) tests were conducted to reveal the phase composition of CC-v-MnO_2 and CC-m-MnO_2. As shown in Fig. 1b, the XRD pattern of carbon cloth exhibits typical characteristics of amorphous carbon material featuring a broad peak centered at about 26° [28]. The XRD patterns of CC-v-MnO_2 and CC-m-MnO_2 show additional diffraction peaks corresponding to α-MnO_2. We note that the diffraction peaks of α-MnO_2 in the XRD pattern of CC-v-MnO_2 are stronger than that in CC-m-MnO_2, indicating the presence of more crystallized α-MnO_2 produced in the CC-v-MnO_2 composite. Notably, the preparation procedure of CC-m-MnO_2 is easier and more feasible for large-scale production (Fig. S2 in Supporting information).

Scanning electron microscope (SEM) and transmission electron microscope (TEM) observations were further performed to reveal the surface morphology and inner microstructure of CC and two CC-MnO_2 composites. As can be seen from SEM images of two CC-MnO_2 composites (Figs. S3a-c in Supporting information), the interwoven structure of CC is well maintained after oxidation. No noticeable morphological differences are observed between CC and two CC-MnO_2 composites at low magnification (Figs. S3d-f in Supporting information). At large magnifications, distinct surface morphologies are observed. The pristine CC shows a smooth surface of carbon fibers with a diameter of 6–8 μm (Fig. S4a in Supporting information). The CC-m-MnO_2 demonstrates a coating layer over the carbon fiber surface, as indicated by the broken region highlighted by the red arrow (Fig. S4b in Supporting information). The CC-v-MnO_2 displays many nanoflakes grown at the carbon fiber surface with a thickness of several nanometers and a lateral size of ~100 nm (Fig. S4c in Supporting information). Notably, if the CC surface is not modified with the oxygen-containing group, many

tiny nanoparticles are produced on the surface (Fig. S5 in Supporting information). This may be ascribed to the weak reactivity between the pristine CC and $KMnO_4$.

TEM was further conducted to characterize the internal microstructures of two CC-MnO_2 composites. As shown in Fig. 1c, the low-magnified TEM image of the CC-v-MnO_2 composite demonstrates nanoflakes vertically grown on the surface of carbon fibers, with a thickness of several nanometers and lateral size of ~50 nm. The high-resolution TEM image and the associated selected area electron diffraction (SAED) pattern show the good crystallinity of the as-produced nanoflakes (Fig. 1d). The lattice fringes with an interlayer space of 0.24 nm correspond to the (330) crystal plane of α-MnO_2 (Fig. 1e). In contrast, the CC-m-MnO_2 product shows a typical coating layer on the carbon fiber surface (Figs. 1f and g). The high-resolution TEM image shows good crystallinity, as confirmed by the SAED patterns in the inset (Fig. 1h). The clear lattice fringes also correspond to the (330) crystal plane with an interlayer space of 0.24 nm.

We assembled half-cells to study the Li plating/stripping in the CC-MnO_2 hosts. The morphology and microstructure of the CC-MnO_2 hosts after lithiation were examined by SEM and TEM. Interestingly, after lithiation to a low potential of 0.12 V, there is an obvious morphology change from a thin layer coating to a nanoflake array (Figs. S6a-e in Supporting information). Such morphology transformation is supposed to be caused by stress-induced structure rearrangement [29]. Upon full discharge, more nanoflakes were clearly observed (Fig. S6f in Supporting information). The microstructure of two CC-MnO_2 composites after full lithiation was further examined by TEM. The above-mentioned morphological transformation is also observed in the TEM image. Numerous nanoflakes with a thickness of ~10 nm and lateral size of ~100 nm at the CC surface are observed (Fig. S6g in Supporting information). These nanoflakes are composed of numerous nanocrystallines (Fig. S6h in Supporting information). The corresponding SAED pattern is well indexed to the (511), (330), and (221) crystal planes of cubic Mn, indicating the reduction of MnO_2 to metallic Mn (Fig. S6i in Supporting information) [30]. Moreover, it can be observed from Fig. S7 (Supporting information) that the nanoflake array morphology of CC-v-MnO_2 can be well preserved during lithiation.

As shown in Figs. 2a-d, the SEM images of the CC-m-MnO_2/Li composite at a lithium deposition capacity of 10 mAh/cm^2 and after full stripping indicate that a dendrite-free smooth morphology is preserved even at high-capacity lithium deposition. As highlighted by red circles in Fig. 2b, some nanoflakes are randomly distributed on the deposited lithium surface. It indicates the expandable feature of the 3D nanoflake array. The presence of Mn-based nanoflakes above the deposited lithium is also confirmed by the energy-dispersive X-ray spectroscopy (EDS) mapping. We can observe the dense distribution of Mn elements along the contour of the carbon fibers (Fig. S8 in Supporting information). In contrast, the intensity of the Mn element signal is very weak in EDS mapping of the CC-v-MnO_2/Li composite at the same lithium deposition capacity of 10 mAh/cm^2 (Fig. S9 in Supporting information). Additionally, after the complete lithium stripping, the morphology of nanoflake arrays recovers (Figs. 2c and d). Such mechanical breathing behavior of the 3D nanoflake array is beneficial for continuously guiding uniform lithium deposition.

To further verify the Mn distribution in the above-mentioned CC-v-MnO_2/Li and CC-m-MnO_2/Li composites, we performed XPS depth analysis. As shown in Fig. 2e, no Mn signal is observed at the surface of the CC-m-MnO_2/Li composite. Prominent B and F signals are detected before Ar^+ sputtering, which can be assigned to the SEI at the anode surface (Fig. 2f and Fig. S10 in Supporting information). After a sputtering of 30 s, a prominent signal of Mn appears, indicating the existence of Mn below the SEI layer.

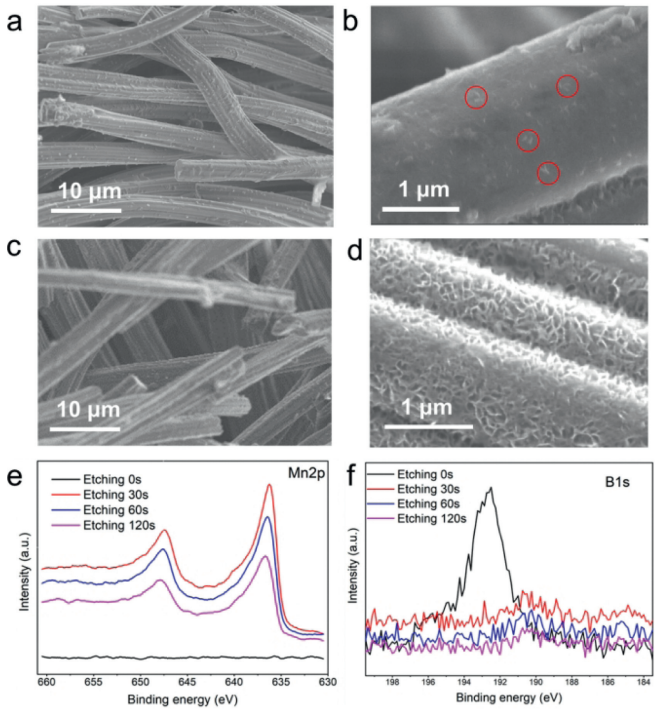


Fig. 2. SEM images of the CC-m-MnO_2/Li composite (a, b) at a lithium plating capacity of 10 mAh/cm^2 and (c, d) after full lithium stripping. Depth profiles of XPS measurement of (e) Mn 2p and (f) B 1s spectra in the CC-m-MnO_2/Li composite.

The B and F signals are not detected, suggesting the sputtering had passed through the SEI layer. As the sputtering goes on, the intensity of characteristic peaks of Mn becomes weaker and weaker. In contrast, almost no Mn signal is detected with the prolonged sputtering time in the CC-v-MnO_2/Li composite (Fig. S11 in Supporting information). Such XPS depth profiling confirms the expansion of Mn/Li_2O arrays and the moving of Mn/Li_2O nanoflakes from the carbon fiber surface to the deposited lithium surface upon lithium plating in the CC-m-MnO_2/Li composite, while the Mn/Li_2O array keeps static over lithium plating on the CC-v-MnO_2/Li composite.

To illustrate the efficient guiding effect of the expandable nanoflake arrays, we simulated the distributions of the electric field of bare Li and the modified Li anode after the formation of Li nuclei by COMSOL Multiphysics. As shown in Fig. S12a (Supporting information), the CC-m-MnO_2/Li anode shows an evenly distributed electric field. No hotspot or tip effect can be observed at the Li nuclei surface. As shown in Fig. S12b (Supporting information), the electric field around the lithium nuclei of the bare Li metal anode is drastically enhanced in certain regions (red color), which is derived from the well-known tip effects. This means Li-ion flux is more readily adsorbed to the projecting nuclei and can increase dendritic development and SEI breakage. The simulation suggests that expandable nanoflake arrays of the CC-m-MnO_2/Li anode are more favorable for promoting uniform Li plating/stripping.

Symmetrical Li/Li cells were fabricated to investigate the Li plating/stripping properties of the CC-v-MnO_2/Li and CC-m-MnO_2/Li electrodes. Figs. S12c and d (Supporting information) compare the galvanostatic cycling of the CC-m-MnO_2/Li and CC-v-MnO_2/Li symmetric cells at a Li deposition capacity of 1.0 mAh/cm^2 and an areal current density of 5 mA/cm^2, respectively. We observe that the CC-m-MnO_2/Li-based cell shows considerably lower voltage polarization of ~50 mV and an extended cycling lifespan (750 cycles) with no noticeable voltage fluctuation or rise in voltage polarization, suggesting its superior electrochemical stability. In contrast,

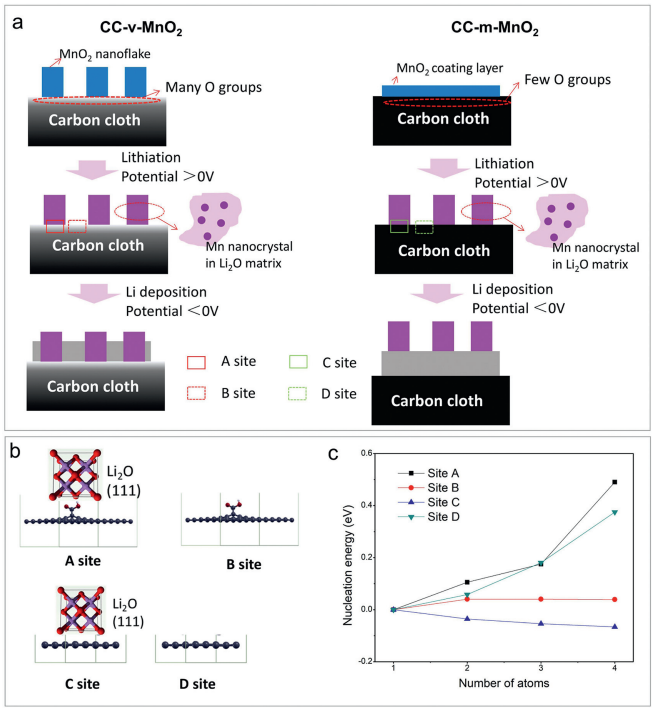


Fig. 3. (a) Schematic illustration of lithiation of and lithium deposition in the CC-v-MnO_2 and CC-m-MnO_2 hosts. (b, c) DFT calculation of the Li nucleation energies at different sites.

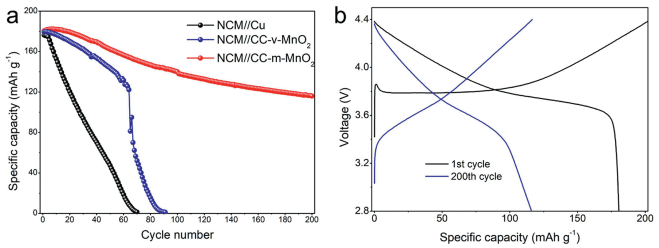


Fig. 4. (a) Cycling performances of NCM//Cu, NCM//CC-v-MnO_2, and NCM//CC-m-MnO_2 based AFLMB at 0.5 C. (b) Charge/discharge curves of the NCM//CC-m-MnO_2 anode-free cell at the 1st and 200th cycle.

the potential of the CC-v-MnO_2/Li-based cell is stable at ~150 mV in the initial 30 h but gradually increases in the following charge-discharge cycles. After cycling for 45 h, obvious voltage reduction is observed, suggesting severe Li dendrite growth and local short circuits. Subsequently, voltage fluctuation and more severe polarization are detected, indicating the poor electrochemical stability of the CC-v-MnO_2/Li electrode. Li plating/stripping reversibility was evaluated by assembling Li/Cu and Li/CC-m-MnO_2 half cells. As we can see in Fig. S13 (Supporting information), the Li/Cu cell shows an average Li plating/stripping Coulombic efficiency of 98.2% at a current density of 0.5 mA/cm^2 and Li plating/stripping capacity of 1 mAh/cm^2. And the Li/CC-m-MnO_2 cell shows a boosted average Coulombic efficiency of 98.9%.

The final morphology of Li plating is highly dependent on nucleation and growth behavior in the initial stage. This can be a crucial factor affecting the dendritic formation. After lithiation, MnO_2 in the CC-MnO_2 composites was converted to Mn nanocrystals embedded in the Li_2O matrix [31]. Each composite thus provides different sites for lithium nucleation and deposition, *i.e.*, the carbon surface and the carbon/Li_2O interface (Fig. 3a). These different sites are expected to show different nucleation energies for lithium nucleation and deposition. We thus further conducted theoretical calculations to study the mechanism of lithium nucleation/growth on CC-m-MnO_2 and CC-v-MnO_2.

The carbon surface of CC-v-MnO_2 has abundant carboxyl (−COOH) functional groups, while the CC-m-MnO_2 shows few oxygen functionalities. Therefore, a graphene basal plane (site D) and carboxyl-bonded graphene basal plane (site B) were used to model the carbon surfaces of CC-m-MnO_2 and CC-v-MnO_2, respectively. Likewise, the graphene basal plane/Li_2O interface (site C) and carboxyl-bonded graphene basal plane/Li_2O interface (site A) were used to model the interfaces of CC-m-MnO_2 and CC-v-MnO_2, respectively (Fig. 3b). Nucleation energy was then estimated to forecast the initial nucleation behavior of lithium. As exhibited in Fig. 3c, a negative value suggests that the nucleation process is thermodynamically favorable and *vice versa*. We found that the bare graphene basal plane (site D) shows a positive and high nucleation energy, indicating unfavorable Li nucleation. Meanwhile, the nucleation energy is significantly reduced to negative values at the graphene basal plane/Li_2O interface (site C). This results in lithium nucleation and subsequent deposition under the Mn/Li_2O nanoflake array. In contrast, the carboxyl-bonded graphene basal plane (site B) shows nucleation energies near zero, much lower than the bare graphene basal plane due to the lithiophilicity of carboxyl groups. However, the nucleation energies are much higher at the carboxyl-bonded graphene basal plane/Li_2O interface (site A). That largely explains why lithium deposits over the Mn/Li_2O nanoflake array in CC-v-MnO_2/Li. To summarize, the CC-v-MnO_2 composite can induce uniform Li nucleation but is not able to guide even lithium growth. In contrast, the CC-m-MnO_2 composite can work as an efficient lithium host to guide uniform Li nucleation and growth by the lithiophilic nanoflake array breathing on the 3D lithium host.

To verify the practical viability of the CC-m-MnO_2 lithium host, AFLMB was assembled with NCM532 as the cathode and 3D Li host of CC-m-MnO_2 as the "anode". Note that the initial discharge and charge capacities of the CC-m-MnO_2 host are determined to be 49 and 37 mAh/g, respectively, with an irreversible capacity of 12 mAh/g (Fig. S14 in Supporting information). It corresponds to a tiny areal capacity loss of 0.11 mAh/cm^2 based on the areal mass density of 9.1 mg/cm^2. The NCM532 cathode owns a high areal mass loading of ~20 mg/cm^2 and a theoretical areal capacity of 3.5 mAh/cm^2. The initial charge/discharge curve of the NCM532 cathode was plotted in Fig. S15 (Supporting information), showing an initial Coulombic efficiency of 82%. This corresponds to an irreversible areal capacity of 0.63 mAh/cm^2. It can be compensated for the first-cycle Li loss for the CC-m-MnO_2 host and subsequent-cycle Li loss by Li plating/stripping. The NCM532 cathode also shows excellent cycling stability with 91% and 82% capacity maintained over 200 cycles at 0.5 C and 1 C, respectively (Fig. S16 in Supporting information).

Fig. 4a compares the cycling performances of AFLMBs with various current collectors of Cu foil, CC-v-MnO_2, and CC-m-MnO_2. We found that the Cu foil-based AFLMB shows stable specific capacities of ~180 mAh/g at the initial five cycles, which subsequently drop rapidly to 50 mAh/g after 51 cycles because of irreversible Li plating/stripping. The CC-v-MnO_2-based AFLMB shows a similar capacity variation trend. However, the capacity decay rate is much slower, with 122 mAh/g retained after 64 cycles, revealing the advantage of 3D hosts for facilitating reversible Li plating/stripping. Note that an abrupt capacity decay is observed at the 65th cycle. The voltage fluctuation in the charge curve indicates the local short circuit (Fig. S17 in Supporting information). Subsequently, the capacity declined remarkably fast to near zero over 25 cycles. More impressively, the CC-m-MnO_2-based AFLMB demonstrates stabilized capacity in the initial ten cycles, which slowly dropped in the following cycles, maintaining 64% of the initial capacity after 200

cycles. The charge/discharge curve in Fig. 4b also does not show significant voltage polarization or fluctuation, suggesting remarkable electrochemical stability. Considering the high working voltage utilized and no external pressure applied in this study, such cycling performance is among the best of reported AFLMB systems with modified current collectors (Table S2 in Supporting information) [32–36].

In summary, we have developed a dense MnO_2 nanoflake array grown on carbon cloth as a "breathable" 3D current collector for stable AFLMB. Such a MnO_2 nanoflake array can transform into an expandable Li_2O/Mn nanoflake array after the initial lithiation. Spectroscopy measurements and theoretical simulations have revealed the preferential deposition at the carbon/Li_2O interface, thereby guiding uniform lithium nucleation and growth. The dendrite-free structure was observed even at a high lithium deposition capacity of 10 mAh/cm^2. The as-constructed AFLMB based on such a current collector shows 64% capacity retention over 200 cycles, among the best cycling performances for AFLMBs with modified current collectors. This work thus provides new insights into the rational design of novel current collectors with mechanical breathing capability for long-life AFLMBs.

Declaration of competing interests

The authors declare that they have no known competing financial interests or personal relationships that could have appeared to influence the work reported in this paper.

CRediT authorship contribution statement

Jiaojiao Deng: Writing – review & editing, Writing – original draft, Visualization, Validation, Software, Methodology, Investigation, Formal analysis, Data curation, Conceptualization. **Haocheng Li:** Writing – review & editing, Validation, Methodology, Data curation. **Fei Zheng:** Writing – review & editing, Validation, Methodology. **Qingsong Weng:** Writing – review & editing, Validation, Methodology. **Yu Bai:** Writing – review & editing, Visualization, Methodology. **Xiaoliang Yu:** Writing – review & editing, Writing – original draft, Validation, Supervision, Resources, Investigation, Funding acquisition, Formal analysis, Conceptualization. **Qianlin Zhang:** Writing – review & editing, Writing – original draft, Supervision, Resources, Methodology, Funding acquisition, Conceptualization. **Qinghua Liang:** Writing – review & editing, Writing – original draft, Supervision, Resources, Funding acquisition, Conceptualization. **Baohua Li:** Writing – review & editing, Writing – original draft, Validation, Supervision, Conceptualization.

Acknowledgment

The authors gratefully acknowledge financial support from the National Natural Science Foundation of China (Nos. 11921006 and 52402052), Inner Mongolia Key R&D and Achievement Transformation Plan (No. 2023YFHH0062), Research Team Cultivation Program of Shenzhen University (No. 2023QNT007). Qinghua Liang acknowledges the financial support from Ganjiang Innovation Academy, Chinese Academy of Sciences.

Supplementary materials

Supplementary material associated with this article can be found, in the online version, at doi:10.1016/j.cclet.2024.110681.

References

[1] J. Liu, Z. Bao, Y. Cui, et al., Nat. Energy 4 (2019) 180–186.
[2] P. Albertus, S. Babinec, S. Litzelman, A. Newman, Nat. Energy 3 (2018) 16–21.
[3] J. Qian, B.D. Adams, J. Zheng, et al., Adv. Funct. Mater. 26 (2016) 7094–7102.
[4] S. Nanda, A. Gupta, A. Manthiram, Adv. Energy Mater. 11 (2021) 2000804.
[5] S. Ding, Z. Fang, L. Zhang, et al., J. Colloid Interface Sci. 672 (2024) 543–551.
[6] L. Sheng, Q. Wang, X. Liu, et al., Nat. Commun. 13 (2022) 172.
[7] C. Liao, R. Zou, J. Zhu, et al., Small 20 (2024) 2305085.
[8] J. Xiao, Science 366 (2019) 426–427.
[9] Y. Liu, D. Lin, Z. Liang, et al., Nat. Commun. 7 (2016) 10992.
[10] S. Liu, K. Jiao, J. Yan, Energy Storage Mater 54 (2023) 689–712.
[11] Z. Wang, L.P. Hou, Z. Li, et al., Carbon Energy 5 (2022) e283.
[12] S. Zhang, B. Cheng, Y. Fang, et al., Chin. Chem. Lett. 33 (2022) 3951–3954.
[13] J.X. Guo, F. Jiang, N.L. Shen, et al., ACS Energy Lett. 9 (2024) 4800–4809.
[14] J. Qian, W.A. Henderson, W. Xu, et al., Nat. Commun. 6 (2015) 6362.
[15] G. Huang, J. Han, F. Zhang, et al., Adv. Mater. 31 (2019) 1805334.
[16] P. Xue, S. Liu, X. Shi, et al., Adv. Mater. 30 (2018) 1804165.
[17] C. Wang, C. Yang, Y. Du, et al., Adv. Funct. Mater. 33 (2023) 2303427.
[18] Y.S. Feng, Y.N. Li, P. Wang, et al., Angew. Chem. Int. Ed. 62 (2023) e202310132.
[19] Y.L. Ye, Y. Zhou, H. Ye, F.F. Cao, J. Energy Chem. 101 (2025) 744–750.
[20] Y. Zhao, Z. Liu, Z. Li, et al., Energy Mater. 2 (2022) 200034.
[21] Y. Gu, W.W. Wang, Y.J. Li, et al., Nat. Commun. 9 (2018) 1339.
[22] X.B. Cheng, S.J. Yang, Z. Liu, et al., Adv. Mater. 36 (2024) 2307370.
[23] G. Zheng, S.W. Lee, Z. Liang, et al., Nat. Nanotechnol. 9 (2014) 618–623.
[24] J. Yang, T. Feng, C. Zhi, et al., J. Colloid Interface Sci. 599 (2021) 819–827.
[25] J. Yan, F.Q. Liu, J. Gao, et al., Adv. Funct. Mater. 31 (2021) 2007255.
[26] M. Su, Y. Chen, S. Wang, H. Wang, Chin. Chem. Lett. 34 (2023) 107553.
[27] V. Tucureanu, A. Matei, A.M. Avram, Crit. Rev. Anal. Chem. 46 (2016) 502–520.
[28] B. Manoj, A.G. Kunjomana, Int. J. Electrochem. Sci. 7 (2012) 3127–3134.
[29] H. Sun, G. Xin, T. Hu, et al., Nat. Commun. 5 (2014) 4526.
[30] L. Li, A.R.O. Raji, J.M. Tour, Adv. Mater. 25 (2013) 6298–6302.
[31] Q. Li, H. Li, Q. Xia, et al., Nat. Mater. 20 (2021) 76–83.
[32] O. Tamwattana, H. Park, J. Kim, et al., ACS Energy Lett. 6 (2021) 4416–4425.
[33] L. Lin, L. Suo, Y.S. Hu, et al., Adv. Energy Mater. 11 (2021) 2003709.
[34] P. Liang, H. Sun, C.L. Huang, et al., Adv. Mater. 34 (2022) 2207361.
[35] S.S. Zhang, X. Fan, C. Wang, Electrochim. Acta 258 (2017) 1201–1207.
[36] A.A. Assegie, C.C. Chung, M.C. Tsai, et al., Nanoscale 11 (2019) 2710–2720.